Double β decays of ^{100}Mo and ^{150}Nd

A. De Silva, M. K. Moe, M. A. Nelson, and M. A. Vient
Department of Physics & Astronomy, University of California, Irvine, California 92697
(Received 12 June 1997)

The double β decays of ^{100}Mo and ^{150}Nd were studied in a time projection chamber located 72 m underground. A 3275-h exposure of a 16.7-g sample of metallic Mo enriched to 97.4% in ^{100}Mo resulted in a two-neutrino half-life, $T_{1/2}^{2\nu}=(6.82^{+0.38}_{-0.53}\pm 0.68)\times 10^{18}$ y. Similarly, a 6287-h exposure of 15.5 g of Nd_2O_3 enriched to 91% in ^{150}Nd yielded $T_{1/2}^{2\nu}=(6.75^{+0.37}_{-0.42}\pm 0.68)\times 10^{18}$ y. Lower limits on half-lives for neutrinoless decay with and without majoron emission also have been measured. [S0556-2813(97)01911-0]

PACS number(s): 21.10.Tg, 23.40.−s, 27.60.+j, 27.70.+q

I. INTRODUCTION

Double β decay, the single isobaric jump of two units in atomic number,

$$(A,Z)\rightarrow(A,Z+2)+2e^{-}+2\overline{\nu_e},$$

is a rare second-order weak transition, directly measurable under favorable circumstances by means of the ejected pair of β particles. The phenomenon has been observed, with its two accompanying neutrinos ($\beta\beta_{2\nu}$), in several nuclei for which single β decay is strongly inhibited or energetically forbidden [1]. The search for a variation lacking the usual pair of neutrinos in the final state is under way in several laboratories as a uniquely sensitive probe of the mass and charge conjugation properties of the neutrino. Should a neutrinoless double β decay ($\beta\beta_{0\nu}$) branch be seen, it would demonstrate that at least one neutrino is a massive Majorana particle [2], at variance with the lepton-conserving, massless Dirac particles of the standard model.

A second nonstandard mode sometimes considered is neutrinoless decay with majoron emission ($\beta\beta_{0\nu,\chi}$). The majoron is a hypothetical boson, coupling to the neutrino with sufficient strength in recent models to make a significant contribution to the $\beta\beta$-decay rate [3–6].

The three decay modes are distinguishable experimentally by the spectrum of the sum of the two β-particle energies. The $\beta\beta_{0\nu}$ mode is characterized by a distinctive line spectrum at $Q_{\beta\beta}$, whereas the $\beta\beta_{2\nu}$ electron sum spectrum is a broad distribution, peaking at about 1/3 of the $Q_{\beta\beta}$ value. The various proposed $\beta\beta_{0\nu,\chi}$ spectra are also broad distributions, generally distinct from $\beta\beta_{2\nu}$.

While all $\beta\beta$ decays observed by direct counting experiments have had the features of standard $\beta\beta_{2\nu}$, stringent lower limits on $\beta\beta_{0\nu}$ and $\beta\beta_{0\nu,\chi}$ half-lives have been achieved. Geochemical and radiochemical $\beta\beta$ experiments and searches for γ rays following $\beta\beta$ decay to excited levels of the daughter do not distinguish among decay modes, but when their rates have been compared with direct-counting limits on the exotic modes, a predominance of $\beta\beta_{2\nu}$ has always been implied [7].

The extraction of upper limits on neutrino mass and neutrino-majoron coupling strength (or of actual values for these parameters, should the $\beta\beta_{0\nu}$ and $\beta\beta_{0\nu,\chi}$ half-lives ever be measured) depends on complicated nuclear matrix element calculations. The comparison of theoretical and experimental half-lives for the observed $\beta\beta_{2\nu}$ mode is an important test for these calculations [1].

Here we describe our final measurements [8] of two relatively fast $\beta\beta$ emitters, ^{100}Mo ($Q_{\beta\beta}=3034\pm 6$ keV) and ^{150}Nd ($Q_{\beta\beta}=3367.1\pm 2.2$ keV) [9]. We also discuss the disappearance of a persistent excess of high-energy $\beta\beta_{0\nu,\chi}$-like events that were present in our earlier data.

II. EXPERIMENTAL APPARATUS

A. Time projection chamber

The measurements were carried out in a time projection chamber (TPC) located in an underground valve house in a canyon wall at the Hoover Dam. This site provided a minimum of 72 m of rock shielding and reduced the cosmic ray muon flux by a factor of approximately 130 from that at the Earth's surface.

The TPC has been described in detail in Refs. [10,11]. It is a rectangular polycarbonate (Lexan) box of inside dimensions $88\times 88\times 23$ cm^3. The $\beta\beta$ source plane bisects the volume into two 10-cm-deep drift regions and serves as the central drift-field electrode. Planes of sensing wires parallel to the source are located near the TPC walls. Anode and cathode wires are mutually perpendicular and provide x and y coordinates. The z coordinate is provided by the arrival time of drifting ionization electrons at the anode. Spatial resolution in x and y is determined by the wire spacing, 5.1 mm. The 5.0-mm z resolution is established by the 5-mm/μs drift velocity and 1-MHz frequency of wire readout. The corresponding 1-μs ''time buckets'' are clocked into an 80-deep shift register, in which the full 10-cm drift distance spans the first 20 buckets. The remaining 60 buckets are used to record any hits that occur in the 1 ms following the initial trigger. This scheme permits tagging background from ^{214}Bi events by recording the subsequent 164-μs ^{214}Po α particle. The required drift field is established by a negative potential applied to the source plane. Drift-field and anode-wire potentials are compensated continuously for fluctuations in barometric pressure. The geometry of the source and wires is illustrated in Fig. 1.

The TPC is shielded on all sides by 15 cm of lead. Notoriously radioactive materials, such as circuit board, solder, ribbon cable, circuit components, and connectors, are all

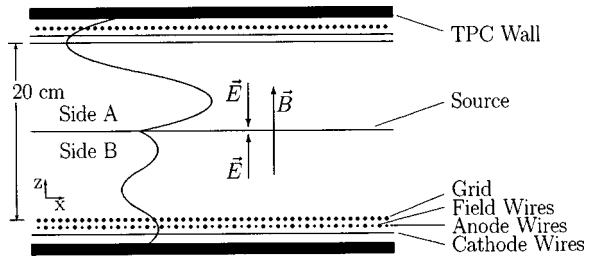

FIG. 1. Schematic representation of the source plane and wire array geometry. The sinusoids represent the x-z view of helical tracks from two electrons emitted by the source.

completely outside the lead shield. Interleaved with the lead shielding are six cosmic-ray veto panels in a 4π arrangement that identifies muon-associated events at a rate of approximately 0.25 Hz.

A magnetic field is applied perpendicular to the source plane by a pair of coils mounted in an iron flux return. An electron emitted from the source follows a helical trajectory about the z axis. The momentum of the particle and its angle to the magnetic field are determined from the parameters of the helix fitted to its track. The 1200-G field (approximately twice the strength in our earlier experiments without the flux return) is uniform to $\pm 0.8\%$ over the active volume of the TPC.

Helium mixed with 7% propane flows through the chamber at a rate of 57 l/hr. Mixture proportions and flow rate are both controlled by a mass-flow controller system. Prior to mixing, the helium is passed through a liquid-nitrogen cold trap, which freezes out all measurable Rn produced by Ra within the gas supply cylinders.

The trigger used in the present experiment requires a start hit and at least one hit in buckets 3–5. In addition to complete tracks, the trigger will capture tracks having a z component as short as three time buckets. This feature increases the efficiency at which short α-particle tracks are saved, while maintaining some protection from noisy wires. Here we refer to α particles other than the ^{214}Po type already included in the 1-ms sensitive period following a ^{214}Bi trigger. An α particle appearing within an hour or two at the site of a $\beta\beta$ candidate event is a good indicator that the event was background from one of the primordial decay chains. The trigger fires at about 0.6 Hz.

A small dead time in the chamber arises primarily from the cosmic ray veto. Triggers are vetoed for a period of 30 μs following a hit in any of the veto panels. The resulting dead time is about 0.6%. The overall dead time of the system is $(0.87 \pm 0.05)\%$.

The data acquisition system is able to direct the latch modules to disable the occasional noisy wire. Typically, the TPC is operated with about 1% of the wires dead or disabled.

Routines for off-line selection of one- and two-electron events are discussed in Sec. VII. Only those $2e^-$ pairs with electrons emerging from opposite sides of the source are analyzed.

B. Isotope preparation

The molybdenum, enriched to 97.4% in ^{100}Mo, was purchased as MoO_3 from a German supplier and is of Russian origin. The oxide is not the optimum form for detection of α particles associated with background processes. As an example, the 7.7-MeV ^{214}Po α-particle range is diminished from about 22 mg/cm^2 in the metal to about 10 mg/cm^2 of Mo in the oxide. For this reason, the MoO_3 was reduced to the metal in our laboratory in a quartz tube in a high-temperature hydrogen atmosphere. About 20.0 g of fine metallic powder were available for source fabrication.

The ^{150}Nd consisted of 3 g of Nd_2O_3 purchased from the same German supplier plus an 82-g batch of Russian Nd_2O_3 obtained through an agreement with the late Professor A. A. Pomansky of the Institute for Nuclear Research (INR) in Moscow. Elemental Nd is reactive, so it was left as the oxide.

Samples of both isotopes were forwarded to Pacific Northwest Laboratories (PNL) for photon counting and mass spectroscopy. The PNL results indicated radioisotopes of europium in the ^{150}Nd at levels too great for $\beta\beta$-decay studies. The INR and commercial batches of neodymium oxide then were sent to the Ames Laboratory Materials Preparation Center, where they were combined and processed with a liquid chromatography system. The ^{150}Nd isotopic enrichment of the combined batches was 90.9%. Of the initial 85 g of Nd_2O_3, 94% survived the purification process. We retained 21.6 g and the balance was returned to Pomansky for his own $\beta\beta$ measurements [12]. Samples were again forwarded to PNL where post-purification measurements indicated a reduction of more than two orders of magnitude in europium contamination [13]. This reduction was more than sufficient, although we were requested not to reveal the level of sensitivity of the measurements. Uranium and thorium were not detected.

Meanwhile, our portion of the Nd_2O_3, which had been stored in sealed plastic bags, changed color from its characteristic robin's-egg blue to a blue-gray. This indicated that some of the oxide had been hydrated to $Nd(OH)_3$. This compound is undesirable for the same reasons discussed in the case of the ^{100}Mo oxide. The hydrate was transferred to a quartz crucible and heated to 1100 °C in an electric furnace. This restored the characteristic blue color, and the approximately 12% loss in mass observed is consistent with conversion of $Nd(OH)_3$ to Nd_2O_3. After processing, approximately 19.0 g remained. It was stored in an evacuated jar until needed.

C. Source preparation

A thin layer of ^{100}Mo was deposited on each of two 4-μm aluminized polyester (Mylar) substrates, each supported by a half section of a Lexan source frame assembly. A nitrogen gas powered gun was used to inject the powdered isotope material at high speed into a glass box positioned in turn over each substrate. The resulting cloud of powder settled onto the Mylar, leaving a thin, uniform deposit of isotope. This fragile layer of powder was then fixed to the Mylar with a fine misting of polyvinyl acetal resin (Formvar) solution. A 1-pCi droplet of ^{207}Bi solution was applied to the geometrical center of one of the source halves in a 3-cm square region left devoid of powder by a mask. After drying, the Bi was fixed in place with a drop of Formvar solution to prevent migration to the $\beta\beta$ deposit. (The conversion electrons emitted by the ^{207}Bi provide a continuous monitor of detector performance.) When dry, the two substrates were placed face

TABLE I. Ranges and escape probabilities for several important α particles. Values in parenthesis for ^{214}Po refer to α-decay identification probability when ''blips'' from shakeoff electrons are used in addition to full α-particle tracks. Energies are taken from Kaplan [14]. Measured P_α values from Ref. [8] have been corrected for loss of ^{214}Bi events when the α comes within ~ 15 μs and spoils the β track, or comes after the 1024-μs window.

			Estimated escape probability P_α (%)			
	α energy	Mean range	^{100}Mo source		^{150}Nd source	
α decay	(MeV)	in air (cm)	Measured	GEANT	Measured	GEANT
^{214}Po	7.6804 ± 0.0009	6.907 ± 0.006	73 ± 5	75	72 ± 5	76
			(98 ± 2)		(85 ± 7)	
^{212}Bi	6.0466 ± 0.0027	4.730 ± 0.008	60 ± 7[a]	65	58 ± 7[a]	66
^{212}Po	8.7801 ± 0.0040	8.570 ± 0.007	79 ± 4[a]	79	78 ± 4[a]	80

[a]Scaled from the ^{214}Po measurement by the Bragg-Kleeman approximation for α-particle ranges in materials.

to face to form a sandwich of Mylar and isotope, with the isotope in the interior and the aluminized surface of the Mylar facing outward.

All seams between the Mylar and the Lexan frame were sealed with low-activity epoxy, isolating the interior of the source from the TPC gas. The interior of the source was vented to atmosphere through an oil bubbler, allowing the slight overpressure of the TPC to press the sheets of source Mylar tightly together into a thin, flat plane. Both the ^{100}Mo and ^{150}Nd $\beta\beta$ sources were prepared in the same manner. The masses of the isotope deposits on the two sources were 16.7 ± 0.1 g of Mo and 15.5 ± 0.1 g of Nd_2O_3. Full details of the source preparation procedure may be found in Ref. [8].

III. DETECTOR PERFORMANCE

A. α-particle detection probability

Detection of α particles is an important aid in identification of $\beta\beta$-decay backgrounds. Source thicknesses were chosen to ensure that a large fraction of α particles would escape to the chamber gas where they would be observed. The probability P_α that an α particle from the source will enter the TPC gas has been calculated with the CERN Library GEANT Monte Carlo program. P_α was also measured for the case of the ^{214}Po α particle, following an injection of ^{222}Rn of sufficient strength to overwhelm pre-existing activity. Here $P_\alpha(^{214}\text{Po})$ was taken as the number of single electrons of energy greater than 1.5 MeV (essentially all were ^{214}Bi β particles) that had an α track in the following millisecond, divided by the sum with or without an α particle. The ^{214}Bi from the Rn injection settles on the source surface, but as long as the source thickness is less than the α-particle range, P_α determined in this way is a good approximation for ^{214}Bi located anywhere on or within the source. The results are given in Table I.

To the extent that ^{214}Bi is on the surface of the source ($\approx 100\%$ for Mo and $\approx 50\%$ for Nd, Sec. VI A), the ^{214}Po α decay can be identified with higher efficiency than implied by these escape probabilities. For surface ^{214}Bi, even the α particle that buries itself completely in the source is nearly always accompanied by ''shakeoff'' electrons, which produce a one- or two-bucket ''blip'' at the x,y location of the decay. Observation of such a blip in the 1-ms post-trigger interval identifies the trigger event as a ^{214}Bi decay. This association is confirmed by the delay-time distribution of blips, which shows the characteristic 164-μs half-life of ^{214}Po.

Since the blips substantially increase the identification chances for the ^{214}Po α particle (see Table I) they are also used in the routine rejection of ^{214}Bi. The α detection enhancement from shakeoff electrons on the ^{150}Nd source is smaller because of subsurface ^{226}Ra. Other α decays used for background estimation are ^{212}Bi and ^{212}Po, also included in Table I.

B. Opening angle acceptance

The TPC's inability to reconstruct tracks making angles to the magnetic field with cosines near 0 or 1, the requirement that electrons from a $\beta\beta$-decay emerge from opposite sides of the source, and multiple scattering of the electrons within the source all conspire to distort the measured opening angle distribution and obliterate the distinction between opening angle distributions for $\beta\beta$ decay and background. We do not make use of opening angle information in our present analysis.

However, it is worth pointing out that the requirement for opposite-side electrons leads to low efficiency for small opening angles and thereby helps suppress one of the potential $\beta\beta$-decay backgrounds, Möller scattering (see Sec. VI). Möller opening angles are in the range $\cos\vartheta_M \approx +0.2$ to $+0.5$. The efficiency for reconstructing events in this range is relatively low and will selectively suppress Möller events.

C. Energy resolution

A convenient line source for displaying energy resolution is ^{207}Bi, which provides internal conversion (IC) energies at approximately 0.5, 1.0, and 1.7 MeV. A separate source assembly was built and peppered with 16 deposits of ^{207}Bi totaling 6 nCi, distributed over the area normally covered with powdered $\beta\beta$-decay isotope.

The resulting energy spectrum of 7×10^5 events is shown in Fig. 2. Energies of electrons with tracks nearly parallel to the magnetic field ($|\cos\vartheta| > 0.8$) are less well determined and have been excluded from this spectrum. The widths of the peaks are determined by fitting each of them with a pair of Gaussians, centered on the K and L lines. The corresponding σ is 26 keV, 39 keV, and 68 keV for the 482-keV, 976-keV,

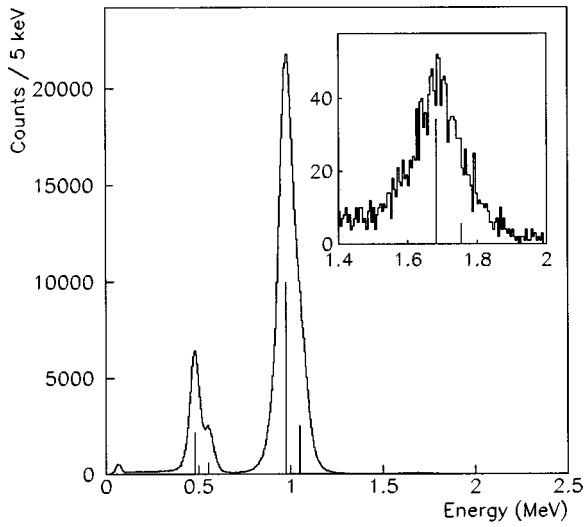

FIG. 2. Measured energy spectrum of 7×10^5 ^{207}Bi IC electrons. The inset shows the weak peak near 1.7 MeV. Electrons with tracks nearly parallel to the magnetic field lines ($|\cos\vartheta|>0.8$) have been cut. Conversion line energies and relative strengths are represented by vertical lines.

and 1682-keV K lines, respectively. The width of each conversion line can be measured at various cosines and a model of resolution versus cosine and energy can be constructed. Figure 3 shows the results of this analysis. This function provides a statistical estimate of the uncertainty in the energy of a given electron track. The Monte Carlo program, described in Sec. III E, uses this function to randomly smear the energies of the simulated events.

D. Energy threshold

The energy of a particle is determined by fitting a helix to the reconstruction of its trajectory. Low-momentum particles will create helices of relatively small radius and low pitch. As the diameter of the helix approaches the x and y resolution of the TPC, the quality of the reconstruction diminishes. Similarly, if the z separation of adjacent cycles of the helix is less than the z resolution of the TPC, the helix will not be resolved.

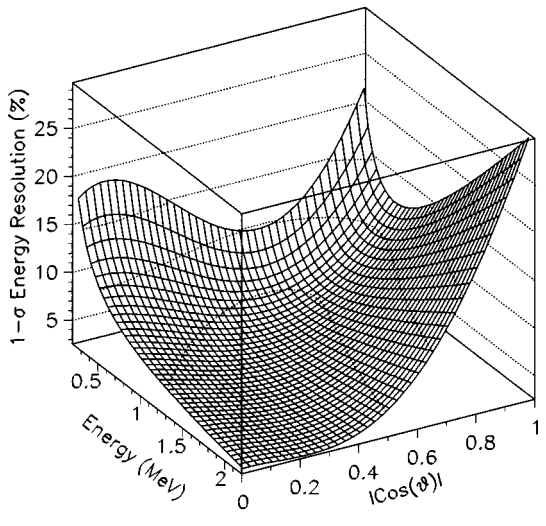

FIG. 3. Energy resolution (in percent) of the TPC as a function of electron energy and the cosine of the angle that the electron makes with the magnetic-field lines. This function is derived from studying the conversion lines of ^{207}Bi.

Although some sensitivity clearly remains for energies as low as the 57-keV ^{207}Bi Auger electron [11], for this analysis a 250-keV energy threshold was imposed. The TPC does not reach optimum efficiency until somewhat higher energies, but in place of still higher-energy cuts, which would sacrifice a significant amount of good data, a model of the detector response was determined and used in subsequent analyses.

Also included in the model is the high-energy response, which is limited as well, because the pitch and radius of the track tend to increase with higher energies. At some point, the track becomes too straight for the fitter to determine reliable helix parameters. Fortunately, a large fraction of events satisfy the requirements for good fits and can be very nicely reconstructed.

E. Detector response model

One could determine the detector response to a particular β spectrum by placing a calibrated β source in the TPC and noting the ratio of the measured spectrum to the true spectrum as a function of energy. Such a function would not be generally applicable, however, because its dependence on the energy derivatives cannot be extracted from a single test spectrum. For this reason, it is useful to separate the detector effects into two classes, intrinsic and instrumental, and deal with the former by Monte Carlo methods. The intrinsic effects include scattering and energy loss of electrons within the $\beta\beta$ source and backscattering of electrons from the TPC walls. Instrumental effects begin with the collection of ionization electrons from the gas and include such factors as the sampling cell size, electron attachment by impurities, gas amplification, the readout electronics, and track reconstruction software.

Intrinsic effects were modeled with the GEANT code. The model could then be applied generally for any β spectrum. More importantly, the model can predict *two-electron* behavior where the electrons are correlated in energy and opening angle as, for example in $\beta\beta$ decay or Möller scattering.

Instrumental effects are too complicated for a reliable Monte Carlo simulation. Their two consequences are the resolution function, already determined from ^{207}Bi measurements in Sec. III C, and the probability that an electron that has already survived the GEANT process for intrinsic effects will also survive the track reconstruction process. Since this probability is the same for any electron emerging from the source with a given energy and polar angle, it can be deduced from a comparison of a TPC-measured β spectrum with the resolution-smeared output of the corresponding intrinsic-effects Monte Carlo calculation. This was done with the equilibrium ^{90}Sr and ^{90}Y combination β spectrum.

Input electrons for the Monte Carlo calculation were sampled from the ^{90}Sr and ^{90}Y spectra of Ref. [15]. The output energies then were smeared by the resolution function of Sec. III C. A comparison with the spectrum of reconstructed electrons from a calibrated drop of ^{90}Sr solution applied to a dummy $\beta\beta$ source in the TPC revealed the sur-

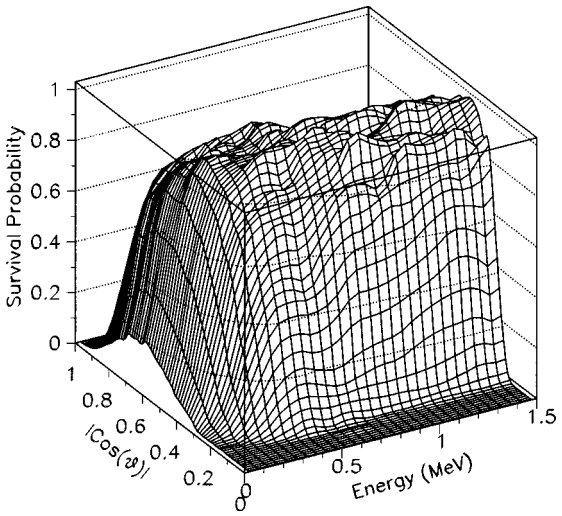

FIG. 4. Normalized detector response as a function of energy and cos(ϑ), the angle between the track and the magnetic field. This is the electron survival probability after its emergence from the source plane.

vival probability of an electron after emerging from the source plane (Fig. 4). This survival probability, extrapolated for energies above 1.5 MeV, was then included in the GEANT Monte Carlo program and used to regenerate the ^{90}Sr lone-electron spectrum; the results compared with the corresponding measured spectrum are shown in Fig. 5.

Measured $2e^-$ events, generated by Möller scattering in the source plane, can also be compared with the simulated results. The ratios of scanned $2e^-$ events to lone-electron events, both taken from measured ^{90}Sr decays, were calculated at nine single-electron thresholds. As seen in Fig. 6, the measurements are in agreement with the Monte Carlo. Also from this figure, a systematic uncertainty of 10% can be estimated and is applied to all Monte Carlo results involving electrons.

IV. TESTS OF DETECTOR RESPONSE MODEL

A. Efficiencies for e^- and $2e^-$ measured with ^{207}Bi

The response model of the preceding section can be used to calculate several specific detection efficiencies that can be tested by direct measurement, as summarized in Table II. The calibrated ^{207}Bi source, at the center of the ^{150}Nd isotope deposit, has an activity of 140.0 ± 4.0 decays per hour. Given the conversion rate of the 1064-keV γ ray, a 0.6% loss due to electron tracks spoiled by x rays and Auger electrons,

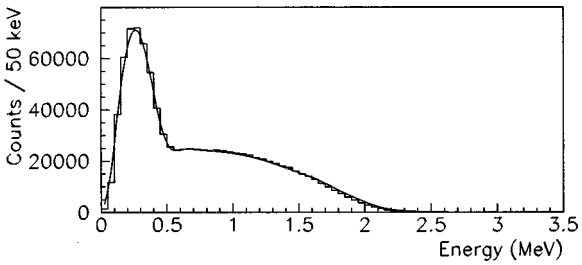

FIG. 5. Measured ^{90}Sr lone-electron spectrum (histogram) and the simulated spectrum (solid line). The simulation includes energy smearing and the detector response model.

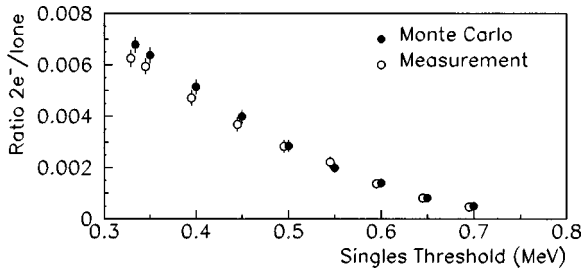

FIG. 6. Ratio of ^{90}Sr $2e^-$ Möller events to lone-electron events as a function of single-electron threshold. Polar angles (ϑ) are restricted to $|\cos\vartheta|<0.8$. The measured data are shifted by -0.01 MeV for clarity.

and a further 2.2% loss due to an accompanying second conversion electron, 13.4 ± 0.4 single $K,L,M,\ldots$ electrons from the 1064-keV transition can be expected every hour. The same calculation for the 570-keV γ ray gives 2.98 ± 0.09 single electrons per hour. During 6286.6 hours of live time, 39 724 electrons were observed in the energy range expected from conversion of the 1064-keV γ ray and 8907 electrons for the 570-keV transition. Thus an overall single e^- efficiency $\varepsilon_e=(47.2\pm1.2)\%$ can be calculated by combining the number of expected electrons from the two lines and the corresponding number of reconstructed tracks. An independent measurement was made with the much hotter 6-nCi ^{207}Bi source described in Sec. III C. The activity of this uncalibrated ^{207}Bi source was determined from the TPC trigger rate. This method yielded $\varepsilon_e=(48.6\pm0.8)\%$ for the 1-MeV line.

The ^{207}Bi deposit can also be used to determine the $2e^-$ efficiency. The product of the conversion rates for the 0.5- and 1-MeV lines gives the rate of IC-IC pairs as 2.914×10^{-3} per 1-MeV γ ray. This implies that an IC-IC cascade should occur at a rate of 2.157×10^{-3} per ^{207}Bi decay. The activity of the drop on the ^{150}Nd source is 1.05 ± 0.03 pCi, which should give 0.3017 ± 0.009 IC-IC pairs per hour.

^{207}Bi IC-IC decays are easily tagged by their location at the center the source plane. In the scatter plot of Fig. 7, most of the points are IC-IC events, as is evident from the clustering near the 481.7-keV and 975.6-keV conversion energies. These events are selected by a circular cut that includes 99% of the IC-IC signal. Points outside the circle [11] represent Möller scattering of single conversion electrons or single conversion electrons accompanied by a Compton electron from a cascade γ ray.

TABLE II. TPC-measured efficiencies and two-electron events as tests of the Monte Carlo model.

	Single-electron efficiency ε_e (%)		Two-electron efficiency ε_{ee} (%)	
	Measured	Monte Carlo	Measured	Monte Carlo
^{207}Bi		53.0 ± 0.1		13.9 ± 0.1
1 pCi	47.2 ± 1.2		13.6 ± 0.9	
6 nCi	48.6 ± 0.8		Two-electron events	
^{214}Bi	53.8 ± 1.6	54.6 ± 0.2	59 ±8	52.9 ± 3.4

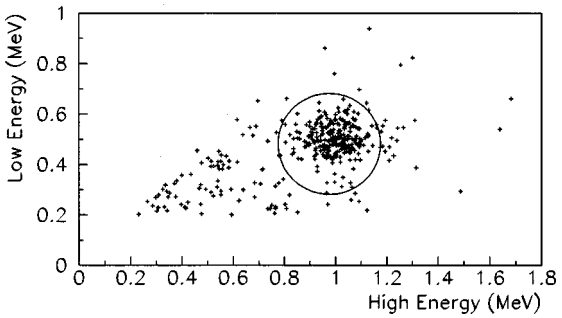

FIG. 7. Scatter plot of electron energies for events in the ^{150}Nd $2e^-$ data set that emerged near the ^{207}Bi deposit. The circle is centered on 481.7 keV and 975.6 keV (the K conversion energies). Möller and Compton scatterings contribute events outside the circle.

This selection method identified 253 IC-IC events in a live time of 6176.6 h. When compared to the estimated activity of the ^{207}Bi deposit, this rate implies an efficiency of $\varepsilon_{ee}=(13.6\pm0.9)\%$.

B. Efficiencies for e^- and $2e^-$ from ^{214}Bi decay

A TPC measurement of the ^{214}Bi β spectrum (Fig. 8) provides another efficiency check. Approximately 1 nCi of ^{222}Rn was injected into the TPC to produce a deposit of daughter products, including ^{214}Bi, on the source plane. The requirement of a spatially correlated α particle in the millisecond following the trigger was used to select triggering ^{214}Bi events, without regard to the quality of the β tracks. From the resulting 46 151-event sample, the single-electron analysis software (Sec. VII) reconstructed 9561 events originating on the source plane with energies above 500 keV.

Corrections were made for the energy cut (51.9%) for β tracks spoiled by overlapping α tracks with a short delay (3.0%), β tracks spoiled by IC's, etc. (2.2%), β tracks originating on the TPC walls $(28.2\pm2.3)\%$, and β particles failing to escape the source and contribute to the 46 151-event sample $(8.1\pm0.8)\%$. The resulting single-electron efficiency is $\varepsilon_e=(53.8\pm1.6)\%$

From the 46 151 ^{214}Bi decays the off-line analysis reconstructed a total of 189 $2e^-$ events (Fig. 9). A single-electron threshold of 400 keV then was imposed to avoid ^{214}Pb contamination. The 64 above-threshold events were individually examined and 59 good $2e^-$ events were identified.

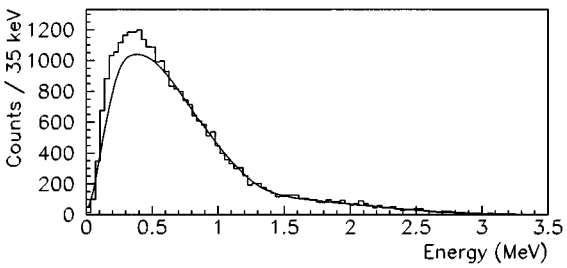

FIG. 8. TPC-measured ^{214}Bi β-decay energy spectrum following ^{222}Rn injection. The solid curve is the GEANT Monte Carlo prediction normalized above 0.5 MeV. The difference arises largely from contamination of the event sample by ^{214}Pb.

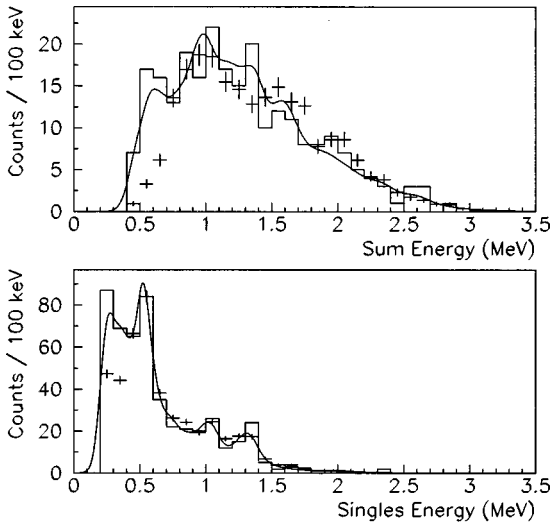

FIG. 9. Measured ^{214}Bi $2e^-$ spectra, satisfying a 0.2-MeV single-electron threshold, following ^{222}Rn injection. The Gaussian ideogram (solid curve) is a better representation of the expected signal than is the histogram. Some ^{214}Pb contamination is present, but is not included in the GEANT Monte Carlo predictions (crosses).

These 59 events included $\beta+$IC, $\beta+$Möller, $\beta+$Compton, etc. (Table III). Unlike the situation in Fig. 7, however, the IC events are not easily isolated and counted. Therefore, a comparison of the $\beta+$IC subset to the number of $\beta+$IC events expected from the decay scheme is not a viable method of calculating the efficiency.

Nevertheless, one can still carry out a meaningful check of the model by directly comparing the 59 measured $2e^-$ events with the total number of all types of $2e^-$ events that the model predicts would be measured from 46 151 ^{214}Bi decays. The overall conversion rate was calculated by incorporating the β, γ, and IC characteristics of the complicated ^{214}Bi decay scheme in a stand-alone Monte Carlo program. This simulation considered more than 99% of the allowed decay channels and estimated the conversion rate to be 0.0194 single conversion electron per ^{214}Bi β decay (Table IV). Feeding this information into the response model, with the usual corrections for wall events and spoiled tracks, resulted in a prediction of 52.9 ± 3.4 $2e^-$ events of all types from the 46 151 decays. The favorable comparison to the 59 measured events is included in Table II.

C. Model testing process

We test the reliability of the Monte Carlo model for efficiency and $2e^-$ event prediction in those specific cases that have been measured directly, namely, ^{207}Bi and ^{214}Bi as described above. The angular distributions and energies of $\beta\beta_{2\nu}$ are replaced in the Monte Carlo model with those for the appropriate isotope. For example, the opening angle distribution for the IC-IC events of ^{207}Bi [16]

$$d\omega/d(\cos\vartheta)\sim1+0.271\cos^2\vartheta$$

and the energies of the two conversion electrons, when inserted in the Monte Carlo method, give ε_{ee} for ^{207}Bi as 13.9 ± 0.1 versus a measured value of 13.6 ± 0.9. The Monte Carlo results and measured values for ε_e and ε_{ee} are sum-

TABLE III. Breakdown of $2e^-$ events, from 10^6 β decays, satisfying a 0.25-MeV single-electron threshold. These were generated by the GEANT model of intrinsic effects using the simulated decay schemes. The columns denote combinations of $2e^-$ events consisting of the beta (β), internal conversion (IC), Möller (M), Compton (C), and photoelectric (P) electrons. $\star=\beta$, IC, M, or C. Columns representing combinations without ten or more events for at least one isotope are omitted, but are included in ''All.'' In columns lacking a β, the β did not escape the source.

	^{100}Mo						^{150}Nd					
Isotope	β+IC	$\beta+M$	$\beta+C$	IC+IC	$P+\star$	All	β+IC	$\beta+M$	$\beta+C$	IC+IC	$P+\star$	All
^{234}Pa^m	548	260	1	0	0	811	546	255	1	0	1	804
^{214}Pb	2568	2	0	0	24	2594	2693	3	0	0	38	2734
^{214}Bi	2163	206	167	14	21	2577	2107	164	151	14	36	2480
^{228}Ac	972	73	50	14	21	1135	995	72	59	18	46	1195
^{212}Pb	10	0	0	0	0	10	6	0	0	0	0	6
^{212}Bi	234	251	9	6	1	503	241	231	17	4	3	497
^{208}Tl	4501	143	204	37	28	4924	4527	113	197	44	78	4966
^{60}Co	0	0	6	0	0	7	0	0	6	0	3	10

marized in Table II. These results are consistent with the 10% systematic uncertainty assigned to the Monte Carlo results in Sec. III E.

V. $\beta\beta_{2\nu}$ EFFICIENCY $\varepsilon_{\beta\beta}$

Determination of the ^{100}Mo and ^{150}Nd half-lives from the observed rates requires knowledge of the $\beta\beta_{2\nu}$ efficiency, $\varepsilon_{\beta\beta}$. Since there is no direct way to measure $\varepsilon_{\beta\beta}$, it must be estimated by the Monte Carlo method. The code employs the detector response model (Sec. III E) and utilizes the opening angle and energy distributions expected for $\beta\beta_{2\nu}$ in the Primakoff-Rosen approximation [17]. The Monte Carlo–generated efficiencies, as a function of the single-electron threshold, are shown in Fig. 10.

VI. BACKGROUNDS

Candidates for $\beta\beta$ decay are characterized by two negative electrons with a common point of origin on the $\beta\beta$ source. Although this signature rejects the vast majority of events from radioactive impurities, there are certain non-$\beta\beta$ processes that mimic the $2e^-$ topology. These include Möller scattering of single electrons born in the source and β-γ cascades in which a γ ray Compton scatters, produces a photoelectron, or internally converts. (See Table III.) Pair production (e^+e^-) is not a background since the helical track of the positron would be rejected by a pitch of the wrong sign.

Dominant among these mechanisms is β decay accompanied by an internal conversion (β+IC), a relatively common phenomenon in the ^{238}U and ^{232}Th decay chains. These families always are present at some level in the $\beta\beta$ isotope stock. In addition, daughters of gaseous ^{220}Rn or ^{222}Rn can migrate to the $\beta\beta$ source surface from Ra impurities elsewhere in the chamber or in the gas-handling system.

The decay chains supply the major radioactivity feeding the other background processes as well. Fortunately, each of these chains contains one or more isotopes with unique and identifiable decay characteristics, so good estimates of total uranium and thorium contamination can be made from the observed activity.

TABLE IV. Properties of isotopes in the U and Th decay chains capable of producing high-energy β+IC events. ''Total'' includes events with one or more conversion electrons and ''Single'' indicates one conversion electron only. These are the raw conversion rates derived from Monte Carlo simulations of the decay schemes, without reference to the TPC.

	Q value	IC per β decay (%)	
Isotope	(MeV)	Total	Single
^{234}Pa^m	2.29	1.27	1.18
^{214}Pb	1.02	40.6	35.1
^{214}Bi	3.27	1.95	1.94
^{228}Ac	2.14	80.3	67.5
^{212}Pb	0.573	41.5	40.2
^{212}Bi	2.25	0.343	0.339
^{208}Tl	4.99	7.07	6.91

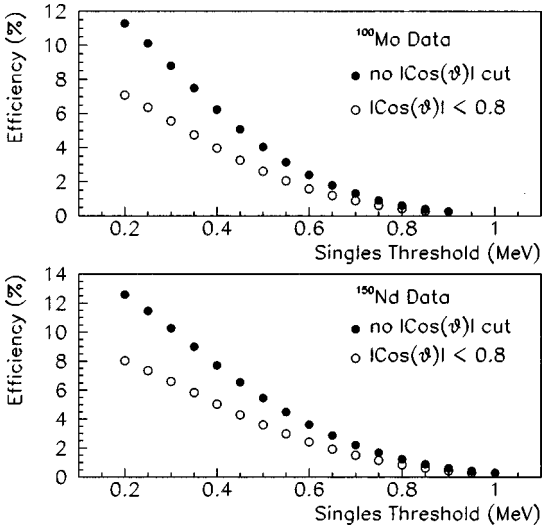

FIG. 10. Efficiency $\varepsilon_{\beta\beta}$ as a function of the single-electron threshold. The statistical uncertainties are negligible compared to the 10% systematic uncertainty (not shown).

A. Uranium series

The uranium chain includes several isotopes with high enough Q_β values to be of concern. A summary of those producing $\beta+$IC events is given in Table IV.

Activity below ^{230}Th is quantified by the characteristic 164-μs β-α sequence from ^{214}Bi and ^{214}Po (''BiPo'' events). The TPC's 1-ms trigger duration includes 99% of the ^{214}Po decays. α tracks that extend into the TPC gas are recorded and stored along with the β tracks responsible for the triggers.

The ^{100}Mo source showed a low level of ^{214}Bi events distributed over the entire source plane, irrespective of the region where the ^{100}Mo was located. This uniformity suggests that very little of the activity in the ^{100}Mo runs arose from contamination of the isotope material. Increased TPC gas flow rates were accompanied by fewer observed ^{214}Bi decays. The flow dependence implied that the primary source of ^{214}Bi in the ^{100}Mo data set was ^{222}Rn in the chamber gas. Data collected during the ^{150}Nd runs indicate that the Nd_2O_3 itself harbored additional ^{214}Bi activity roughly equal to that from ^{222}Rn contamination of the chamber gas.

1. ^{214}Bi and ^{214}Pb backgrounds

^{214}Bi is potentially the single most dangerous background. The $2e^-$ sum-energy spectrum collected during the ^{222}Rn-injection runs (Fig. 9) is not unlike the expected $\beta\beta_{2\nu}$ signal. The α particles and shakeoff electrons from decay of the ^{214}Po daughter are exploited to tag ^{214}Bi events with good efficiency (Sec. III A). The number of tagged events together with the known tagging efficiency $P_\alpha(^{214}\mathrm{Po})$ give an accurate measure of the number of untagged ^{214}Bi events remaining in the data:

$$N_{\mathrm{untagged}} = N_{\mathrm{tagged}}(1+\xi)\frac{1-\eta P_\alpha(^{214}\mathrm{Po})}{P_\alpha(^{214}\mathrm{Po})},$$

where $\xi = 0.081$ and $\eta = 0.987$ are corrections for corruption of Bi events by Po α's in the first 15 μs or for Po decays beyond the 1024-μs window. We found that we could also tag ^{214}Bi events by one or more of the three *previous* links in the uranium chain, with about 50% efficiency in the more difficult ^{150}Nd case. The number of ^{214}Bi events remaining after the primary ^{214}Po tag, however, was already so small (Table V) that this more tedious procedure was not needed.

Although it has only a 1.0-MeV Q value, ^{214}Pb has a very high IC probability which makes it a major source of low-energy background. The ^{214}Pb $\beta+$IC single-electron- and sum-energy spectra were measured with the same ^{222}Rn injection data used to measure the ^{214}Bi spectrum in Sec. IV B. In this case, however, only manually scanned events with no accompanying α-particle or shakeoff electron were considered. This sample contains less than 2% contamination by ^{214}Bi events.

The ^{214}Pb/^{214}Bi ratio of $2e^-$ events from Table III was used to determine the number of ^{214}Pb events in the $\beta\beta$ data set from the number of tagged plus untagged ^{214}Bi events discussed above. (As a check, this ratio, measured from the ^{222}Rn injection data at a 0.200-MeV single-electron threshold, is 2.51 ± 0.30, in agreement with the corresponding Monte Carlo value of $2.82 \pm 0.07 \pm 0.40$.)

TABLE V. Summary of $2e^-$ $\beta\beta$-decay background events. ^{228}Ac, ^{212}Pb, and ^{212}Bi contamination are estimated from ^{208}Tl activity (see Sec. VI B). Also listed are Möller scattering contributions as estimated from lone-electron energy spectra. ''Cuts'' include a 250-keV single-electron threshold and 4-wire radius of exclusion about the ^{207}Bi spot at the center.

		Number of events		
		Tagged		
$\beta\beta$-decay isotope	Background type	Found	Passed cuts	Remain in data
^{100}Mo	^{214}Pb	24	4	0.16 ± 2.09
	^{214}Bi	9	4	0.12 ± 0.11
	^{228}Ac			8.8 ± 3.5[a]
	^{212}Pb			0.08 ± 0.03[a]
	^{212}Bi			0.6 ± 0.2[a]
	^{208}Tl	14	8	5.8 ± 2.6
	Möller			20.5 ± 3.6[a,b]
^{150}Nd	^{214}Pb	76	25	33.3 ± 10.2
	^{214}Bi	61	44	9.0 ± 4.7
	^{228}Ac			11.9 ± 4.4[a]
	^{212}Pb			0.06 ± 0.02[a]
	^{212}Bi			0.8 ± 0.3[a]
	^{208}Tl	25	10	7.9 ± 3.3
	Möller			9.2 ± 3.1[a,b]

[a]Monte Carlo systematic uncertainty included.

[b]Excludes $\beta+$Möller events already included for the above isotopes.

It is possible to identify individually and remove many of the ^{214}Pb events in the $\beta\beta$-decay data set by tagging them with the characteristic BiPo signature that follows with a mean delay of 28.4 min. If a 1-cm^2 area of coincidence and a 2-h search window are assumed, the chance of an accidental coincidence between a $\beta\beta$ event and a ^{214}Bi decay is only about 1 in 500. The search has been carried out on all of the $\beta\beta$ candidates from both sources within the 2-h (six half-life) time period following the candidate. After human confirmation of a valid BiPo tag (Fig. 11) the ^{214}Pb event is removed from the data. Results are shown in Table V.

2. ^{234}Pa^m background

A breach of secular equilibrium could allow a ^{234}Pa^m signal without any ^{214}Bi. Since the Mo refinement and enrichment processes could throw these isotopes out of equilibrium, we must evaluate the level of ^{234}Pa^m contamination by searching for its decays directly. This isotope has only one strong conversion line at 695 keV, so any $2e^-$ contribution should populate the single-electron-energy spectrum at that energy. There is no obvious excess observed at 695 keV in either the ^{100}Mo or ^{150}Nd $2e^-$ single-electron-energy spectrum, so any ^{234}Pa^m contribution is small.

The ^{234}Pa^m events that do occur must be preceded by the low-energy ^{234}Th β particle within several 1.2-min half-lives. Techniques used to tag ^{208}Tl $2e^-$ events will also find this decay sequence with high efficiency (although it would probably be labeled as a ^{208}Tl event). Therefore, background from ^{234}Pa^m is assumed to be negligible.

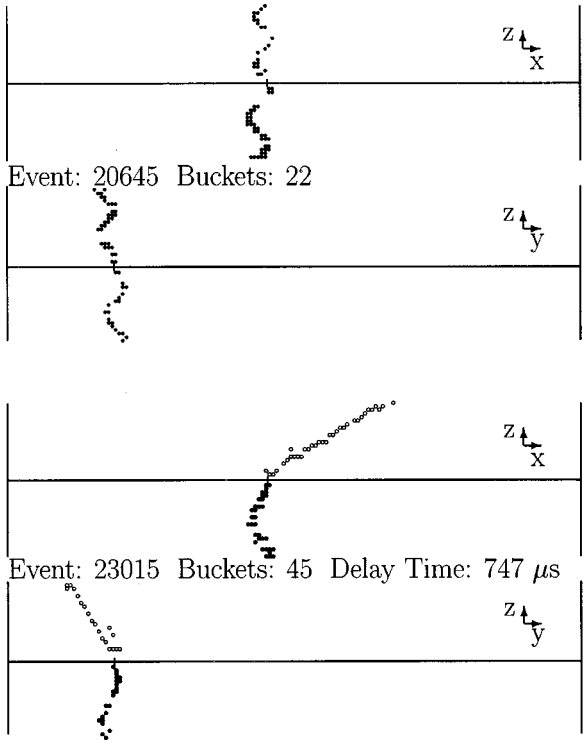

FIG. 11. Example of ^{214}Pb β+IC event identification. The top event is a low-energy $\beta\beta$-decay candidate. The bottom event is a ''BiPo'' sequence emerging from the same point on the source 82 min later, indicating that the candidate is probably a ^{214}Pb β+IC event. Tick marks near the vertex are at the same position in each figure. Open circles are the ^{214}Po α track, 747 μs delayed.

B. Thorium series

The potential of thorium daughters for serious $\beta\beta$ background is evident in Fig. 12, which shows measured $2e^-$ single-electron- and sum-energy spectra for equilibrium ^{212}Pb+^{212}Bi+^{208}Tl, obtained by injecting ^{220}Rn gas into the center of the TPC. Also shown are corresponding spectra generated by a Monte Carlo method. Noticeable in the sum-energy spectrum is a significant population in the 3-MeV region where one looks for $\beta\beta_{0\nu}$ decay in ^{100}Mo and ^{150}Nd.

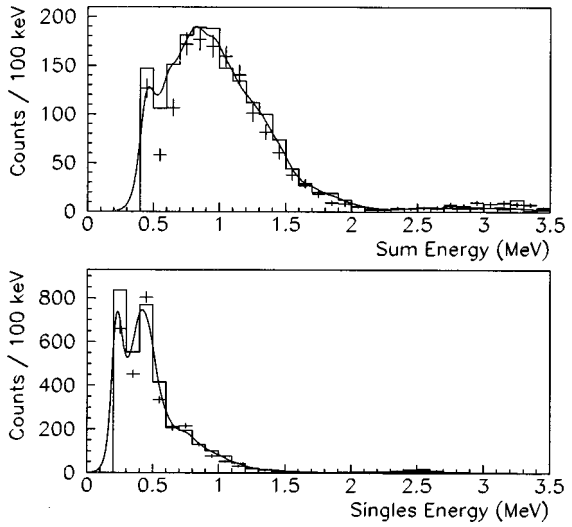

FIG. 12. Measured ^{212}Pb+^{212}Bi+^{208}Tl equilibrium $2e^-$ spectrum, satisfying a 0.2-MeV single-electron threshold, following ^{220}Rn injection. The solid curve is the Gaussian ideogram. The corresponding GEANT Monte Carlo prediction (crosses) includes the branching and loss of ^{212}Bi events spoiled by the ^{212}Po α.

The presence of thorium chain contaminants can be recognized from observation of the 0.3-μs, mass-212 BiPo sequence. Within the temporal resolution of the TPC, both the β and α decays will appear to occur simultaneously and will both be recorded in the trigger hits of the event. This signature can be imitated by $\approx$1% of the ^{214}Bi decays in which the 164-μs α decay of ^{214}Po occurs in the first few microseconds. A small correction for the mass-214 effect can be applied once the uranium chain activity is estimated and does not interfere with using ^{212}Bi as a thorium tracer.

Gas is introduced continuously into the TPC from the top. When 56-s ^{220}Rn is injected into the gas feed line, subsequent activity is localized at the top of the chamber. Since this pattern is not observed in normal data runs, the thorium activity is within the chamber, probably in the $\beta\beta$ source itself.

The serious background isotopes of the thorium series are separated by a maximum half-life of 1.9 y (^{228}Th). Considering the elapsed time between processing and measurement of our isotopes, it is safe to say that the thorium chain from ^{228}Ac to ^{208}Tl is in approximate equilibrium.

1. ^{208}Tl background

With a Q value of almost 5 MeV and 0.5% of its decays generating two electrons passing the standard cuts (Table III), ^{208}Tl is another particularly dangerous background. Fortunately, the highest-energy decays are almost exclusively from internal conversion of the 2.61-MeV γ ray, so events near 3 MeV can be removed by a cut on single electrons near the 2.53-MeV conversion energy.

The use of the mass-212 BiPo count to quantify the activity of the Th series is not as straightforward as in the mass-214 case. The effectively instantaneous ^{212}Po α particle is often lost within the ^{212}Bi β track. It is sometimes possible, however, to identify a $\beta\beta$-decay candidate as a ^{208}Tl event by a back search for the α decay that must precede it with a 3.1-min half-life. For all $\beta\beta$-decay candidate events, the preceding 20 min (six half-lives) is searched by software for any particle originating near the candidate's vertex. Particle identification is left to the person analyzing the data.

The efficiency of this search procedure is the probability of seeing the ^{212}Bi α decay, $P_\alpha(^{212}\mathrm{Bi})$ from Table I. (This search would be enhanced by the conversion electron from the 40-keV level in ^{208}Tl that occurs with 70% of the ^{212}Bi α decays, but because of its low energy this electron rarely reaches the TPC gas.) The corresponding ^{208}Tl count is included in Table V.

2. ^{212}Bi and ^{212}Pb backgrounds

Although Q_β is 2.25 MeV, $2e^-$ production per β decay by ^{212}Bi is only 10% of that by ^{208}Tl (Table III). Branching increases the ^{212}Bi portion to 18%, but finally it is reduced to 4% by corruption from the essentially simultaneous ^{212}Po α

particle, which appears in the gas 80% of the time (Table I). This small background contribution of ^{212}Bi is also included in Table V.

The number of ^{212}Pb $2e^-$ events can be determined from ^{208}Tl decays in a similar manner. The branching fractions and $2e^-$ probabilities predict that ^{212}Pb events should be detected less than 0.6% as frequently as similar ^{208}Tl decays. These are also included in Table V.

3. ^{228}Ac background

The complicated decay scheme of ^{228}Ac almost always produces an internal conversion and will frequently produce *multiple* conversions. Decays with three or more electrons appearing will not be accepted as $\beta\beta$-decay events, so this characteristic helps reduce the probability of ^{228}Ac contributing to the measured $\beta\beta$-decay spectra.

Although the singles-energy Monte Carlo spectrum for ^{228}Ac $\beta+$IC events has a distinctive peak near 0.85 MeV, there is no hint of such a peak in the measured $2e^-$ spectra. We can also scale the ^{228}Ac contribution from the ^{208}Tl activity. Assuming that the thorium chain is in equilibrium, branching fractions and $2e^-$ probabilities predict that ^{228}Ac $2e^-$ events should be detected with $\sim$65% the frequency of similar ^{208}Tl decays. These are also included in Table V.

C. Other sources of conversion backgrounds

Moe and Lowenthal [18] have investigated the possibility of $\beta+$IC backgrounds produced in ^{82}Se by isotopes outside of the natural decay series. They considered nuclei produced from cosmic ray activity, contaminants from atmospheric nuclear weapons test fallout, common man-made materials such as ^{60}Co, and long-lived nonseries isotopes such as ^{40}K. In order to be considered a serious source of $\beta+$IC background, an isotope must have significant internal conversion probability and Q value, a half-life greater than the order of six months, or, alternately, a plausible continuous production mechanism. (We have never seen a $\beta\beta$ candidate rate decline over the duration of the experiment.) None of the nuclides investigated satisfied all of these requirements.

For ^{150}Nd we also considered ^{152}Eu and ^{154}Eu. These were largely removed by the purification at Ames and were not in evidence in the fits discussed in the following section. Similarly, ^{108}Ag^m, sometimes found in ^{100}Mo, was not seen in the fits.

VII. ANALYSIS OF THE DATA

A. Off-line event selection

Each day the data acquisition system recorded about 50 000 events, from which a $\beta\beta$ signal of two or three events had to be extracted. Automated event stripping routines applied a set of empirical criteria engineered to select events that could be $\beta\beta$-decay candidates. A similar set of routines was designed for identifying lone electrons.

B. Event scanning and fitting

1. Lone-electron events

Since ^{100}Mo and ^{150}Nd are stable against single β decay, all lone electrons spawned in the source are due to unwanted radioactivity. Producers of $2e^-$ backgrounds generally emit far more copious numbers of single electrons. Studying the lone electrons[1] emitted from the source plane helps establish limits on the number of associated $2e^-$ background events. This can be accomplished by fitting the lone-electron energy spectrum with component background spectra to estimate each component's activity.

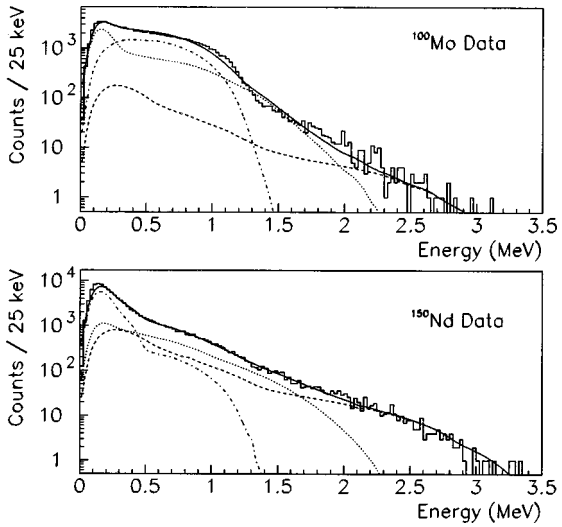

FIG. 13. Histograms of the lone-electron energy spectra from ^{100}Mo and ^{150}Nd runs and their fitted (at $\geqslant$200 keV) background components. These are ^{238}U (excluding ^{234}Pa^m) (dashed curve), ^{232}Th (dotted curve), the sum of ^{40}K, ^{60}Co, and ^{137}Cs (dash-dotted curve), and the total spectrum (solid curve).

Figure 13 shows the energy spectra of lone electrons exclusive of the ^{207}Bi source, collected from all but 518 h of the ^{100}Mo runs and from the entire set of ^{150}Nd runs. These spectra were fitted with various background lone-electron spectra generated by the GEANT Monte Carlo program using Ref. [15] for input spectra. Included were ^{40}K, ^{60}Co, ^{137}Cs, and daughters of the ^{238}U, ^{232}Th, and ^{235}U decay chains. In addition, ^{108}Ag was considered for the ^{100}Mo data while ^{152}Eu and ^{154}Eu were included for ^{150}Nd.

[1]Before his death in 1990, Professor D. Skobeltzin of INR Moscow hoped someone would investigate the anomalous scattering of β particles observed in his early cloud chamber experiments. Suggesting that a He-filled TPC was the ideal detector, Professor G. Zatsepin relayed this wish to us and requested that we publish this footnote. Skobeltzin's photographs (see, e.g., [38]) showed β particles from ^{214}Bi suffering apparent inelastic collisions in which they lost as much as 90% of their energy. As Skobeltzin described it in [39], the phenomenon occurred in 5–10 % of the β tracks within 20 cm of the source and was consistent kinematically with an $\approx 10^{-10}$-s in-flight decay of an unstable particle. We have never observed this effect in the many β tracks examined in the course of our $\beta\beta$ work and would certainly have seen it at the 5–10% level. Nevertheless, to be quantitative, we specifically examined the first 20 cm of 230 high-energy β tracks from the decay of ^{214}Bi. We saw no event with a sudden, large loss of energy. This result rules out more than a 1% effect in our gas mixture, with 90% confidence. Without seeing Skobeltzin's original photographs, we can only speculate that the anomaly resulted from nonuniform illumination of his chamber.

TABLE VI. Activities corresponding to the fit to the ^{150}Nd lone-electron energy spectrum of Fig. 13. Also shown are total $2e^-$ events surviving standard cuts, as calculated from the activity and alternatively from Table V, which is considered to be more reliable.

Isotope	Activity (μBq/g)	Total $2e^-$ events	
		From fit[a]	From Table V
^{234}Pa^m	$\leqslant 18.7^{b}$	$\leqslant 8.7^{b}$	
^{214}Pb	$71.5^{+4.1}_{-4.1}$[c]	$68.5^{+8.0}_{-8.0}$	58.3 $\pm$10.2
^{214}Bi	[c]	$58.3^{+6.8}_{-6.8}$	53.0 $\pm$ 4.7
^{210}Bi	$4.3^{+10.8}_{-0.0}$	0	
^{228}Ac	$98.3^{+14.9}_{-14.7}$[d]	$41.1^{+7.6}_{-7.5}$	11.9 $\pm$ 4.4[a]
^{212}Pb	[d]	$0.21^{+0.09}_{-0.09}$	0.06$\pm$ 0.02[a]
^{208}Tl	[d]	$61.6^{+11.2}_{-11.1}$	17.9 $\pm$ 3.3
^{212}Bi	$20.4^{+4.1}_{-0.2}$	$0.7^{+0.2}_{-0.1}$	0.8 $\pm$ 0.3[a]
^{40}K	$43.7^{+10.5}_{-10.5}$	0	
^{60}Co	613^{+24}_{-24}	$2.1^{+0.7}_{-0.7}$	
^{137}Cs	239^{+10}_{-10}	0	

[a]Monte Carlo systematic uncertainty included.
[b]Limit at 90% confidence level.
[c]^{214}Pb and ^{214}Bi were fitted together.
[d]^{228}Ac, ^{212}Pb, and ^{208}Tl were fitted together.

The fit to the ^{100}Mo spectrum was of limited success. Difficulty reproducing the shoulder near 1.2 MeV is suggestive of a contribution from an unidentified contaminant. We do not consider this fit to be valid. Since the likely heavy elements have been included, the unknown contaminant is not expected to be a strong IC emitter. Its dominant contribution to $2e^-$ background should be Möller scattering, which is accounted for by the lone-electron spectrum, independent of any fit (Sec. VII C).

The fit of the ^{150}Nd spectrum, however, yielded a good match to the measured data. The results are shown in Table VI. Although ^{212}Bi is in equilibrium with the ^{232}Th decay chain, it was fitted as an independent parameter in order to calculate the ^{212}Po α-particle escape probability. This was determined to be $67.5^{+8.2}_{-4.9}$%, consistent with the values listed in Table I.

In addition to the isotopes listed Table VI, others were considered and rejected. Daughters of ^{235}U, specifically ^{211}Pb and ^{207}Tl, were acceptable to the fit, but at the expense of ^{40}K. Ultimately, ^{235}U background was rejected by the fits to the $2e^-$ spectra as discussed in Sec. VII D 2. Similarly, ^{152}Eu was also acceptable in the lone-electron fits but not in the $2e^-$ counterpart. On the other hand, ^{154}Eu was rejected by the lone-electron fit.

2. Two-electron events

The off-line stripper selects negative electron pairs emerging from opposite sides of the source plane. We did not reconstruct same-side events because of added complexity in event selection and fitting, as well as in understanding the associated efficiencies.

The stripper rejects events that are not potential $\beta\beta$-decay candidates. When it cannot reject an event with certainty, it will save it. This system ensures that essentially all recognizable $\beta\beta$-decay events are accepted, and efficiency of the off-line stripper is not an issue. Studies show that the stripper does not reject any events that would not have been rejected by a human scanner.

The off-line stripper saved $2e^-$ ''$\beta\beta$-decay candidate'' events at rate of about 25–30 per day of running. These events were individually studied by a physicist. Events that had the correct $\beta\beta$-decay topology were fitted with two independent helices. The scanning software determined the energy and opening angle of the event based on the parameters of the fit in conjunction with the magnet current, drift field voltage, and atmospheric pressure information recorded with the event.

A 250-keV threshold was imposed on each electron. Two-electron events from the ^{207}Bi deposit (Sec. IV A) were eliminated by excluding electrons within a four-wire radius of the source center.

Occasionally, the fitter had trouble converging to a good fit because of small defects in a visually acceptable track. The scanning software allowed the user to remove these defects. This was done only when necessary and always to the smallest possible extent. In the case of gaps in the track, a single added point usually guided the fitter to the correct result. Ionization electrons formed where the track entered the 5-mm dead space between the TPC wall and the first plane of wires could arrive at the anode a few microseconds later, causing stray hits that could be safely deleted. An electron that scattered abruptly in the gas was usually handled by deleting an entire section of the track, leaving a single sinusoid for the fitter to work on. A status flag was recorded with the fit parameters indicating those few cases where the track was modified.

C. Background identification

The tagging methods described in Sec. VI were used to eliminate, event by event, much of the U- and Th-series background and estimate the number of background events remaining among the $\beta\beta$ candidates. In the ^{100}Mo data set 16 background events were found and in the ^{150}Nd data set 79 events, which otherwise would have been accepted as $\beta\beta$-decay candidates. The energy spectra of remaining events are shown in Figs. 14 and 15. There are 410 remaining $2e^-$ events in the ^{100}Mo data set, while the corresponding number for ^{150}Nd is 476. Table V shows details of how many background counts were identified and also summarizes the expected contamination remaining in the data. The spectra still include the untagged background events listed in the last column of the table.

The expected background contamination for ^{150}Nd can also be estimated from the activity derived from the lone electron fits. GEANT α-particle escape probabilities for ^{212}Po

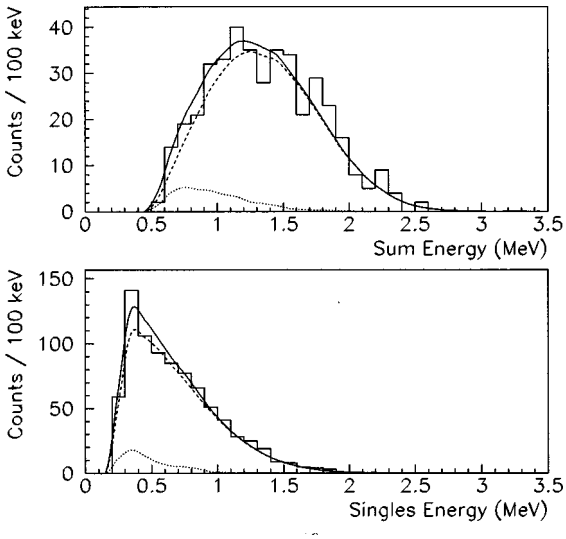

FIG. 14. Histograms of the ^{100}Mo sum- and single-electron-energy spectra for $2e^-$ events with tagged background decays removed. Events represented have single-electron energies greater than 250 keV and originate at least four wires from the ^{207}Bi calibration deposit. Also displayed are the results of the extended maximum likelihood fit where the curves denote total background (dotted), $\beta\beta_{2\nu}$ (dashed), and their sum (solid).

and ^{214}Po (Table I) and $2e^-$ production coefficients (Table III) were used in this calculation. The results, listed in Table VI, are in rough agreement with those in Table V, with the exception of the thorium daughters where the fit is less solid due to the interplay of several constituents in the same energy region. These fit results are not used in our final background estimates, but serve as a rough consistency check of the more precise determinations in Table V.

In addition to U and Th backgrounds, isotopes outside these series contribute $2e^-$ events through the β + Möller process. Möller scattering by the entire lone-electron spectrum can be estimated by Monte Carlo. Since a subset of these Möller events has already been accounted for in the contributions of isotopes listed in Table V, those contributions are subtracted to yield the balance labeled ''Möller'' in the table.

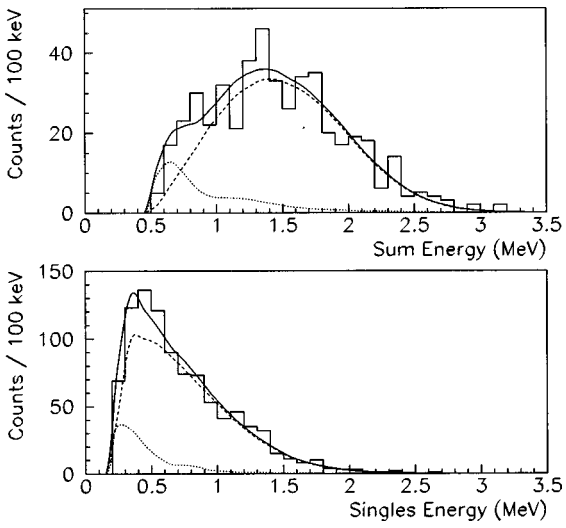

FIG. 15. ^{150}Nd counterpart of Fig. 14.

The method used to estimate the Möller production by the lone-electron spectrum is as follows. The true number of lone electrons $N(K)$, as a function of true energy K, can be obtained from the measured number $N'(K')$, where K' is the measured electron energy. This is given by

$$N(K)=\frac{N'_{\rm shift}(K)}{g(K)}, \tag{1}$$

where

$$N'_{\rm shift}(K)=\int N'(K')\ P(K,K')\ dK',$$

$$g(K)=\frac{N^{\rm MC}_{\rm shift}(K)}{N(K)}.$$

$\int P(K,K')\ dK'=1$ is a probability distribution function, while $N^{MC}_{shift}(K)$ is the number of events surviving; both were determined from Monte Carlo methods using the measured lone-electron-energy spectrum as input. The first iteration true spectrum, obtained in this manner, was input to the Monte Carlo method to obtain the lone and $2e^-$ energy spectra. The former was found to be in excellent agreement with the measured spectrum; thus further iterations were unnecessary.

The total β+Möller contribution, estimated from the Monte Carlo method, is $21.8\pm2.7\pm2.3$ for ^{100}Mo and $13.9\pm2.6\pm1.5$ for ^{150}Nd. The β + Möller events, remaining in the data and listed in Table V, were obtained by subtracting the contribution of each isotope in the table. This contribution was determined by scaling the remaining events by the Monte Carlo determined fraction of β+Möller to total $2e^-$ events.

D. Determination of $\beta\beta$-decay rate

The spectra of $\beta\beta$-decay candidates remaining are composed of real $\beta\beta$-decay events and a residue of $2e^-$ backgrounds. Good half-life determinations depend on accurate appraisals of the signals contained in the spectra. This can be done in several ways.

1. Cuts applied to observed spectra

The majority of $2e^-$ backgrounds occur at low energies and can be greatly reduced by a high single-electron-energy threshold. A Monte Carlo simulation can then be used to estimate the number of events that would survive the cut, allowing us to estimate the number of events in the entire spectrum based on those events over our threshold.

A 500-keV single-electron-energy cut is a reasonable threshold choice, as it eliminates a large portion of the backgrounds while retaining much of the $\beta\beta$ decay. Higher-energy cuts would remove somewhat more background, but they rapidly degrade the statistics of the measured $\beta\beta$-decay spectra. This cut results in estimates for the standard uncut spectrum of 420 ± 34 events in the ^{100}Mo energy spectrum and 480 ± 33 counts in the ^{150}Nd spectrum. (This same cut applied to the $|\cos\vartheta|<0.8$ spectrum implies 407 ± 42 ^{100}Mo events and 423 ± 39 ^{150}Nd events.)

2. Fits to the observed energy spectra

As an alternative to the above method, the data were fitted with the spectra expected from both the signal and the common backgrounds. This technique allows full use of all data.

The procedure employed was the extended maximum likelihood (EML) method [19–21]. EML analysis uses one or more probability distributions that should describe the data in question, each of which has one or more free parameters describing its shape. The parameters are adjusted so that the probability of the data being derived from that distribution is maximized.

For spectral fits, Monte Carlo–generated $\beta\beta$ and background spectra were used as probability distributions, with the only free parameters being their absolute normalizations. Exceptions were ^{208}Tl, ^{212}Pb, and ^{212}Bi for which the measured ^{220}Rn injected spectrum was used.

The likelihood function is given by

$$\mathcal{L}=\left[\prod_i P(x_i,\vec{a})\right]e^{-\mathcal{N}}, \tag{2}$$

where $P(x_i,\vec{a})$ is the probability of observing event x_i, given the distribution described by the parameters $\vec{a}$, and $\mathcal{N}$ is the normalization of the model. More specifically, the probability $P(x,\vec{a})$ is the sum of all the probabilities of the normalized spectra of interest, i.e.,

$$P(x,\vec{a})=\sum_j a_j p_j(x),$$

where

$$\int p_j(x)dx=1.$$

The $p_j(x)$ may include models of a variety of energy spectra, i.e., the $\beta\beta_{2\nu}$-decay sum, $\beta\beta_{2\nu}$-decay single electrons, the $\beta\beta_{0\nu,\chi}$-decay sum, $\beta\beta_{0\nu,\chi}$-decay single electrons, the ^{214}Pb sum, ^{214}Pb single electrons etc. The parameters $\vec{a}$ are then explicitly the absolute normalizations of the various model components, so that

$$\mathcal{N}=\sum_j a_j .$$

When both single-electron- and sum-energy spectra are used in a fit, a single normalization is used to describe both spectra, i.e., there is a single parameter used to describe the number of events attributed to each process. With this scheme, the sum-energy spectrum normalization for a given background process would be a_j, while the normalization of the associated single-electron-spectrum would be $2a_j$.

A fitter was developed for maximizing Eq. (2) based on the CERN Program Library's MINUIT minimization package. The fitter was designed for maximum flexibility and allows the user to select arbitrary combinations of models, apply various cuts to the data, restrict fits to specified energy ranges, and even apply a random smearing of the data for studies of systematic effects.

3. Inclusion of background estimates

One has to choose a reasonable method for applying the various measured and calculated background models. Two extreme possibilities are either to fix all background model normalizations at the best estimates while leaving only the $\beta\beta$-decay model free to fluctuate in the fit or to leave all models completely unconstrained.

Neither of these extremes is particularly appealing. While the background estimates are based on careful measurements, and there is no particular reason to doubt them, the $\beta\beta$ candidate spectrum is, in a sense, an independent measurement of these contamination levels. Fixing the background models at some *a priori* normalization results in total disregard of the background information contained in the measured $2e^-$ spectrum. Similarly, allowing the model normalizations to vary freely ignores the best estimates. In addition, the various background spectra can be qualitatively quite similar (e.g. the ^{214}Bi $2e^-$ sum-energy spectrum and the theoretical $\beta\beta$ decay). These similarities generate correlated parameters in the fitting procedure, adding nonphysical constraints to the problem.

A compromise to these extremes is to suggest the best-estimate values for the various backgrounds to the fitter as initial values and then let the fitter vary the parameters by some amount determined by the uncertainties associated with each. This is relatively easy to do in the extended maximum likelihood scheme since the energy spectra and the background estimations are independent experiments. This means that the corresponding probabilities may be simply appended to the likelihood function. Specifically, the likelihood function is modified to include the probabilities of the background models taking on given normalizations as determined by Gaussian probabilities centered on the best estimates, with standard deviations equal to the measured uncertainties:

$$\mathcal{L}=\left[\prod_i P(x_i,\vec{a})\right]e^{-\mathcal{N}}\left[\prod_j e^{-(a_j-\hat{a}_j)^2/2\sigma_j^2}\right],$$

where the $\hat{a}_j$ are the best estimates for the normalizations of the models, the σ_j are the uncertainties in those estimates, and the a_j are, as before, the fitted parameters representing the normalizations of the models.

The estimates summarized in Table V were used in an EML fit to the $2e^-$ spectra using the procedure described above. The uncertainties in the best estimates were scaled up from the 1σ values quoted in Table V to reflect 90% confidence levels. The only unrestricted parameters were those associated with the $\beta\beta_{2\nu}$ model normalization and the parameters of backgrounds not listed in Table V. The fits were performed on the standard spectra (i.e., no cosine or energy cuts) and consisted of a fit to all events in the sum-energy and single-electron-energy spectra. Table VII summarizes the inputs and results of the fitting procedure.

The uncertainties in the fitted normalizations are calculated by the MINOS routine within the MINUIT minimization package and are derived by considering the shape of the likelihood function near the maximum. This procedure underestimates the uncertainties of the fitted components in Table VII because of the use of both sum and single-electron spectra in the fits. MINOS ''thinks'' it is working with $N+2N=3N$ independent events, but the $2N$ electrons from

TABLE VII. Summary of inputs and results of extended maximum Likelihood fits to the $\beta\beta$-decay $2e^-$ energy spectra. All uncertainties and limits represent 90% confidence levels.

$\beta\beta$-decay isotope	Spectral model	Constrained by $\mathcal{L}$	Initial estimate	Fitted value[a]
^{100}Mo	$\beta\beta_{2\nu}$	no		$376.7^{+20.3}_{-22.4}$
	Möller	yes	20.5 ± 5.9	$19.9^{+3.9}_{-3.9}$
	^{234}Pa	no		$\leqslant 15.6$
	^{214}Pb	yes	0.2 ± 3.4	$\leqslant 2.3$
	^{214}Bi	yes	0.12± 0.17	$0.11^{+0.68}_{+0.11}$
	^{228}Ac	yes	8.8 ± 5.8	$8.5^{+3.9}_{-3.9}$
	^{208}Tl[b]	yes	6.5 ± 4.4	$5.9^{+3.4}_{-3.4}$
	^{211}Pb	no		$\leqslant 8.2$
	^{60}Co	no		$\leqslant 6.3$
^{150}Nd	$\beta\beta_{2\nu}$	no		$414.4^{+22.3}_{-22.4}$
	Möller	yes	9.2 ± 5.1	$8.9^{+3.7}_{-3.7}$
	^{234}Pa	no		$\leqslant 13.0$
	^{214}Pb	yes	33.3 ±16.7	$26.8^{+5.8}_{-5.7}$
	^{214}Bi	yes	9.0 ± 7.7	$9.4^{+4.5}_{-4.5}$
	^{228}Ac	yes	11.9 ± 7.2	$11.2^{+4.4}_{-4.4}$
	^{208}Tl[b]	yes	8.7 ± 5.5	$9.0^{+3.8}_{-3.8}$
	^{211}Pb	no		$\leqslant 5.1$
	^{60}Co	no		$\leqslant 3.6$
	^{152}Eu	no		$\leqslant 5.1$

[a]See discussion of uncertainties in Sec. VII D 3.
[b]Includes ^{212}Pb and ^{212}Bi.

the single-electron spectrum provide no additional information for the overall normalization. We re-estimate the *uncertainty* in the number of $\beta\beta$ events by repeating the fit on the sum spectrum only. The resulting $\beta\beta$ component in this case is similar, so the sum-spectrum uncertainties for $N_{\beta\beta}$ are used in Table VIII and the half-life calculations.

Figures 14 and 15 show the fitted model spectra superimposed on the experimental data. As described in Sec. VII D 2, the fit considers each event independently; the binning shown in Figs. 14 and 15 is for illustrative purposes only.

TABLE VIII. Parameters used in half-life determination. The ''source mass'' is the Mo or Nd_2O_3 material actually used, not just the $\beta\beta$-decay atoms. ''Observed $\beta\beta$-decay events'' are based on maximum likelihood fit to data. Uncertainties are 1σ.

		Parameter value	
Parameter	Description	^{100}Mo run	^{150}Nd run
$\varepsilon_{\beta\beta}$[a]	$2e^-$ efficiency (%)	10.1±0.1	11.5±0.1
$f_{\rm enr}$	isotope enrichment	0.974	0.91
$f_{\rm mol}$	$\beta\beta$ atoms/molecule	1	2
$M_{\rm tot}$	source mass (g)	16.7±0.1	15.5±0.1
$W_{\rm mol}$	molecular wt. (g/mol)	99.91	346.4
N_A	Avogadro no. ($\rm mol^{-1}$)	6.022×10^{23}	
$t_{\rm live}$	Live time (h)	3275±2	6287±3
$N_{\beta\beta}$	observed $\beta\beta$ events	$377^{+21}_{-29}\pm2$	$414^{+23}_{-25}\pm2$

[a]10% systematic uncertainty not included.

4. Systematic uncertainties in EML fit

The EML fit is a point-by-point fit rather than a fit to a binned histogram; this feature makes it simple to estimate the effect of the TPC's energy resolution on the fitted results. The energy of every electron in the data set has an uncertainty associated with it, so by randomly altering each of these energies in keeping with a Gaussian distribution defined by the best-estimate energy and its uncertainty, a hypothetical energy spectrum can be generated from the altered experimental data. This new spectrum can then be analyzed with the EML fitter and will probably produce results slightly different from the unaltered data; these differences are due solely to the energy resolution of the experiment, not the statistics of the data set. This procedure was repeated about 1000 times on both the ^{100}Mo and ^{150}Nd data sets and distributions of $\beta\beta_{2\nu}$ fits were generated. The widths of the distributions were quite small and imply an uncertainty of only about 0.5%.

E. Half-life calculations

The half-life of the $\beta\beta$-decay isotope under investigation is given by the fundamental quantities determined in this experiment as

$$T_{1/2}=\left(\frac{\epsilon_{\beta\beta}}{100}\right) f_{\rm enr}\, f_{\rm mol}\left(\frac{M_{\rm tot}}{W_{\rm mol}}\right)N_A\left(\frac{t_{\rm live}}{N_{\beta\beta}}\right)\ln 2. \qquad (3)$$

The parameters in Eq. (3) are described in Table VIII, which also summarizes their values. Using these values, the EML-based half-lives for the two isotopes studied are

$$T^{2\nu}_{1/2}(^{100}\mathrm{Mo})=(6.82^{+0.38}_{-0.53}\pm0.68)\times10^{18}\ \text{y},$$

$$T^{2\nu}_{1/2}(^{150}\mathrm{Nd})=(6.75^{+0.37}_{-0.42}\pm0.68)\times10^{18}\ \text{y}.$$

A comparison with other experiments can be found in Table IX and with theory in Table X.

The estimated number of $\beta\beta$-decay events based on single-electron energy threshold cuts may also be used in lieu of the EML-based estimates in the half-life calculations. The half-lives derived from those values are plotted in Fig.

TABLE IX. Comparison of the results produced by this work with those from other experiments. Uncertainties and half-life limits are at the 90% (68%) confidence levels. Limits and uncertainties in square brackets indicate that the confidence level was not specified.

$T_{1/2}^{2\nu}$	$T_{1/2}^{0\nu}$	$T_{1/2}^{0\nu,\chi}$	
(10^{18} y)	(10^{21} y)	(10^{20} y)	Work
	^{100}Mo Run		
$6.82^{+(0.38)\pm(0.68)}_{-(0.53)}$	>1.23	>3.31	this work
$7.6^{+(2.2)}_{-(1.4)}$	$>(22)$		[22]
	$>(52)$	$>(54)$	[23]
$9.5\pm[0.4]\pm[0.9]$	>6.4	>5	[24]
$11.5^{+5.4(3.0)}_{-2.8(2.0)}$	>2.6		[25,26]
$3.3^{+(2.0)}_{-(1.0)}$	$>(0.71)$		[27]
	^{150}Nd Run		
$6.75^{+(0.37)}_{-(0.42)}\pm(0.68)$	>1.22	>2.82	this work
$18.8^{+(6.6)}_{-(3.9)}\pm(1.9)$	>0.21	>1.7	[28]
>11			[12]

16. The hatched regions in the figure represent the result of the EML half-life calculation. The EML result agrees well with the the single-electron-energy threshold method near the favored threshold of about 500 keV. This figure does not include systematic errors, which contribute approximately the same uncertainty to each measurement.

F. Kurie plots

The Kurie plots were generated by first subtracting the background $2e^-$ sum energy spectra from the candidate spectrum using the amounts given by the EML fit results. The next step involved obtaining the true $2e^-$ residual spectrum. Here Eq. (1) was used, where K and K' now refer to the true and measured sum energy and

$$g(K)=\frac{N_{\rm shift}^{\rm MC}(K)}{N_\tau(K)},$$

TABLE X. Theoretical half-lives for ^{100}Mo and ^{150}Nd. Zero-neutrino predictions assume $\langle m_\nu\rangle=1$ eV.

Isotope	$T_{1/2}^{2\nu}$ (y)	$T_{1/2}^{0\nu}$ (y)	Ref.
^{100}Mo	$(2.87-7.66)\times10^{18}$	$(2.6-4.7)\times10^{23}$	[29]
	1.13×10^{18}	1.27×10^{24}	[30]
	6.0×10^{18}	1.9×10^{24}	[31]
^{150}Nd		1.05×10^{24}	[32]
	6.73×10^{18}		[33]
	7.37×10^{18}	3.37×10^{22}	[30]

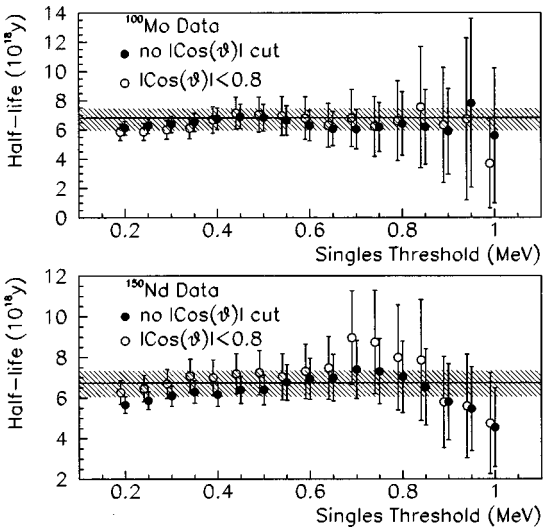

FIG. 16. Graphical representation of half-lives derived from the number of events at various single-electron-energy thresholds. (Open circles are shifted by -0.01 MeV for clarity.) The hatched band represents the result of the EML fit to the energy spectra. Uncertainties are statistical and represent 90% confidence levels; systematic uncertainties contribute approximately 10% in addition to those shown. (One should keep in mind that nearby points are strongly correlated.)

where $N_\tau(K)$ is the true number of events in the sum energy spectrum with single-electron energies greater than 0.25 MeV. Also for this calculation $P(K,K')$ and $N_{\rm shift}^{\rm MC}(K)$ were determined using the theoretical $\beta\beta$ spectrum as input to the Monte Carlo method. (This was later replaced by a randomly generated spectrum in order to determine the systematic uncertainty.) Finally, the Kurie plot values were calculated from the true residual spectrum using the formula [34]

$$(Q_{\beta\beta}-K)\propto((dN/dK)/\{(K-2\tau)[f_0(K)+f_\tau(K)]\})^{1/5},$$

where

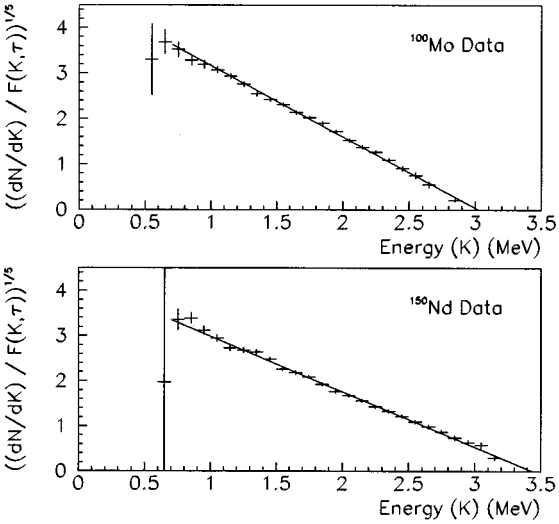

FIG. 17. Kurie plots for ^{100}Mo and ^{150}Nd. Also shown are linear fits to the points and the K intercept indicating the end-point energy. ($F(K,\tau)=(K-2\tau)[f_0(K)+f_\tau(K)]$. See the text.)

$$f_0(K) = K^4/30 + K^3 m/3 + 4K^2 m^2/3 + 2Km^3 + m^4,$$

$$f_\tau(K) = \tau(K-\tau)[K^2/15 + 2Km/3 + 2m^2/3 + \tau(K-\tau)/5],$$

and m is the electron mass. This formula was obtained by including the single-threshold τ and using the Primakoff-Rosen approximation for the Coulomb effect; the approximation produces less than 1% distortion over the plotted range. The Kurie plot (see Fig. 17) projects to an end-point energy for the ^{100}Mo source of $3.03 \pm 0.02 \pm 0.06$ MeV, in good agreement with the mass difference of 3.03 MeV. The corresponding ^{150}Nd value is $3.44 \pm 0.02 \pm 0.06$ MeV, also in agreement with the mass difference of 3.37 MeV.

G. Exotic decay limits

1. $\beta\beta_{0\nu}$-decay half-life limits

The expected $\beta\beta_{0\nu}$ distributions were generated with a Monte Carlo simulation. For ^{100}Mo, the full width at half maximum lies between 2.89 and 3.18 MeV and for ^{150}Nd this region is bounded by 3.21 and 3.54 MeV. There were no counts from either isotope observed within the cut regions and Poisson statistics allows us to reject 2.3 events at the 90% confidence level.

Half-life limits are derived from the above limits by applying Eq. (3). Two of the parameters listed in Table VIII must be altered for this calculation: The 90% C.L. decay limits are used in place of the number of observed decays and a new efficiency for the $\beta\beta_{0\nu}$ case is given by Monte Carlo as $\epsilon_{\beta\beta} = 11.12 \pm 0.07$ for ^{100}Mo and $\epsilon_{\beta\beta} = 11.50 \pm 0.07$ for ^{150}Nd. With these parameters, the half-life limits are (at 90% C.L.)

$$T^{0\nu}_{1/2}(^{100}\mathrm{Mo}) > 1.23 \times 10^{21} \text{ y},$$

$$T^{0\nu}_{1/2}(^{150}\mathrm{Nd}) > 1.22 \times 10^{21} \text{ y}.$$

(See Table X for theoretical predictions.) These $\beta\beta_{0\nu}$ half-lives do not give competitive limits on neutrino mass and right-handed current parameters.

2. $\beta\beta_{0\nu,\chi}$-decay half-life limits

We restrict our analysis to the ''ordinary majoron,'' index equal to 1 in Ref. [6]. Maximum likelihood fits were performed on both the ^{100}Mo and ^{150}Nd data sets, using the same fitting program previously used for the $\beta\beta_{2\nu}$ analysis. In this case, the fit was restricted to energies well above the majority of $\beta\beta_{2\nu}$ backgrounds, where the majoron decay signature is significant (i.e., single-electron energies greater than 750 keV and sum energies greater than 1.5 MeV). The fit was performed jointly over both the sum- and single-electron-energy spectra and included only two models: the $\beta\beta_{2\nu}$ and $\beta\beta_{0\nu,\chi}$ Monte Carlo energy spectra. Under the assumption that poor energy resolution at high energies will adversely effect the reliability of our $\beta\beta_{0\nu,\chi}$ limit estimates, we cut the data at $|\cos\vartheta| < 0.8$.

In both the ^{100}Mo and ^{150}Nd cosine-cut spectra, the EML fitting procedure indicates that the data sample is consistent with there being no $\beta\beta_{0\nu,\chi}$ events in either spectrum. The algorithm used by MINUIT to determine confidence intervals, MINOS, cannot be used when the most likely solution is against a physical boundary (in this case, negative normalizations are nonphysical solutions), so a direct integration of the likelihood function must be performed in order to calculate the confidence intervals.

The 90% confidence limit on the number of $\beta\beta_{0\nu,\chi}$ events in our data sets is 7.76 events in the ^{100}Mo data set and 9.73 events in the ^{150}Nd data set. Half-life limits can be calculated by using Eq. (3) with these decay limits in place of an observed number of decays and using the appropriate $\beta\beta_{0\nu,\chi}$ efficiencies of $\epsilon_{\beta\beta} = 10.13 \pm 0.06$ for ^{100}Mo and $\epsilon_{\beta\beta} = 11.25 \pm 0.07$ for ^{150}Nd, giving

$$T^{0\nu,\chi}_{1/2}(^{100}\mathrm{Mo}) > 3.31 \times 10^{20} \text{ y},$$

$$T^{0\nu,\chi}_{1/2}(^{150}\mathrm{Nd}) > 2.82 \times 10^{20} \text{ y},$$

at the 90% confidence limit. The $\beta\beta_{0\nu,\chi}$ half-life limit published by our group in [11] was based on an analysis of binned data and the fitting routine has since improved. We consider the current analysis to be more reliable. We use the matrix elements of Ref. [30] to put limits on the effective neutrino-majoron coupling constant and obtain

$$\langle g_{\nu,\chi} \rangle (^{100}\mathrm{Mo}) < 6.26 \times 10^{-4},$$

$$\langle g_{\nu,\chi} \rangle (^{150}\mathrm{Nd}) < 9.96 \times 10^{-5},$$

at the 90% confidence level.

VIII. CONCLUSION

Improvements in fitting techniques and in determination of the detector efficiency have resulted in a ^{100}Mo half-life that is markedly shorter than our initial $1.16^{+0.34}_{-0.08} \times 10^{19}$ y estimate [35]. Our use of binned data in the original maximum-likelihood fitting procedure did not make full use of spectral information. This problem is avoided with the unbinned EML procedure employed in the present work. Another factor is the improved calculation and testing of detector efficiency, which is now smaller by 19%.

Although the choice of a very thin source plane precluded sufficient source mass to give competitive limits on $\beta\beta_{0\nu}$, it did result in uncommonly pure $\beta\beta_{2\nu}$ energy spectra. These spectra were produced without need of a dummy source or subtraction of untagged background. The derived Kurie plots are straight over a broad energy range and intercept the energy axis close to the expected $Q_{\beta\beta}$ values.

The present ^{100}Mo half-life supports the quasiparticle random-phase approximation (QRPA) calculation of Ref. [31], with a particle-particle interaction parameter of -390. Likewise, the QRPA result of Ref. [29], with an effective nucleon-nucleon interaction derived from the Bonn one-

boson exchange potential, also agrees with the measurement if one chooses a ten single-particle state basis. Additionally, our result remains consistent with the ''low-lying-state dominance'' conjecture of Ref. [36], when the measured ^{100}Tc electron capture branching of Ref. [37] is employed, and illustrates the rapid convergence of the second-order perturbation expression for the matrix element.

The half-life measured for ^{150}Nd is in excellent agreement with the pseudo SU(3) model of Ref. [33] and favors a deformation parameter β of 0.28. The result also supports the QRPA of Ref. [30], with an effective nucleon-nucleon interaction given by the G matrix of the Paris potential, although this model does less well with ^{100}Mo.

The intriguing high-energy anomalies in our earlier $\beta\beta$-decay sum-energy spectra did not withstand the improved energy resolution that resulted from a doubled magnetic-field strength. No suggestion of $\beta\beta_{0\nu,\chi}$ remains in either sum spectrum. At our level of sensitivity, the double β decay energy spectrum is well described by standard theory.

ACKNOWLEDGMENTS

We express our thanks for the contributions of Steve Elliott and Alan Hahn and for informative discussions with Petr Vogel. We thank Ben Wilkinson, Project Manager at the Hoover Dam, and his successor, Blaine Hamann, for their enthusiastic provision of an underground site for this experiment and we are grateful to Bill Sharp for logistical support at the dam. This work was supported by the U.S. Department of Energy under Grant No. DE-FG03-91ER40679.

[1] M. Moe and P. Vogel, Annu. Rev. Nucl. Sci. **44**, 247 (1994).
[2] B. Kayser, in *Nuclear Beta Decays and Neutrino*, edited by T. Kotani, H. Ejiri, and E. Takasugi (World Scientific, Singapore, 1986), pp. 473–481.
[3] Z. Berezhiani, A. Smirnov, and J. Valle, Phys. Lett. B **291**, 99 (1992).
[4] C. Burgess and J. Cline, Phys. Lett. B **298**, 141 (1993).
[5] C. Burgess and J. Cline, Phys. Rev. D **49**, 5925 (1994).
[6] P. Bamert, C. Burgess, and R. Mohapatra, Nucl. Phys. **B449**, 25 (1995).
[7] M. Moe, Int. J. Mod. Phys. E **2**, 507 (1993).
[8] M. A. Nelson, Ph.D. thesis, University of California, Irvine, 1995.
[9] A. H. Wapstra and G. Audi, Nucl. Phys. **A432**, 55 (1985).
[10] S. Elliott, A. Hahn, and M. Moe, Nucl. Instrum. Methods Phys. Res. A **273**, 226 (1988).
[11] M. Moe, M. Nelson, and M. Vient, Prog. Part. Nucl. Phys. **32**, 247 (1994).
[12] S. I. Vasil'ev *et al.*, JETP Lett. **58**, 178 (1993).
[13] R. L. Brodzinski (private communication).
[14] I. Kaplan, *Nuclear Physics* (Addison-Wesley, Reading, MA, 1955).
[15] *Beta and Antineutrino Radiation of Radioactive Nuclei*, edited by P. Rubtsov (Energoatomizdat, Moscow, 1989).
[16] P. Kleinheinz *et al.*, Nucl. Phys. **A93**, 63 (1967).
[17] H. Primakoff and S. P. Rosen, Rep. Prog. Phys. **22**, 121 (1959).
[18] M. Moe and D. D. Lowenthal, Phys. Rev. C **22**, 2186 (1980).
[19] R. Barlow, Nucl. Instrum. Methods Phys. Res. A **297**, 496 (1990).
[20] L. Lyons, *Statistics for Nuclear and Particle Physicists* (Cambridge University Press, Cambridge, 1986).
[21] J. Orear, University of California, Ernest O. Lawrence Radiation Laboratory Report No. UCRL-8417, 1958 (unpublished).
[22] M. Alston-Garnjost *et al.*, Phys. Rev. C **55**, 474 (1997).
[23] H. Ejiri *et al.*, Nucl. Phys. **A611**, 85 (1996).
[24] D. Dassié *et al.* (NEMO Collaboration), Phys. Rev. D **51**, 2090 (1995).
[25] H. Ejiri *et al.*, Phys. Lett. B **258**, 17 (1991).
[26] H. Ejiri *et al.*, J. Phys. G **17**, S155 (1991).
[27] S. I. Vasil'ev *et al.*, JETP Lett. **51**, 622 (1990).
[28] V. Artemiev *et al.*, Phys. Lett. B **345**, 564 (1995).
[29] J. Suhonen and O. Civitarese, Phys. Rev. C **49**, 3055 (1994).
[30] A. Staudt, K. Muto, and H. V. Klapdor-Kleingrothaus, Europhys. Lett. **13**, 31 (1990).
[31] J. Engel, P. Vogel, and M. R. Zirnbauer, Phys. Rev. C **37**, 731 (1988).
[32] J. Hirsch, O. Castaños, and P. O. Hess, Nucl. Phys. **A582**, 124 (1995).
[33] J. Hirsch, O. Castaños, P. O. Hess, and O. Civitarese, Nucl. Phys. **A589**, 445 (1995).
[34] A. Balysh *et al.*, Phys. Rev. Lett. **77**, 5186 (1996).
[35] S. R. Elliott *et al.*, J. Phys. G **17**, S145 (1991).
[36] J. Abad, A. Morales, R. Nunez-Lagos, and A. F. Pacheco, An. Fis. **80**, 9 (1984).
[37] A. Garcia *et al.*, Phys. Rev. C **47**, 2910 (1993).
[38] D. Skobeltzin, Nature (London) **137**, 234 (1936).
[39] D. Skobeltzin, *Sergei Ivanovich Vavilov* (Academy of Sciences of the USSR, Moscow, 1952).